

1    **Mechanisms driving the dispersal of hydrothermal iron from the northern Mid**  
2    **Atlantic Ridge**

3  
4    Alessandro Tagliabue<sup>1</sup>, Alastair J. M. Lough<sup>2,3</sup>, Clément Vic<sup>4</sup>, Vassil Roussenov<sup>1</sup>,  
5    Jonathan Gula<sup>4,5</sup>, Maeve C. Lohan<sup>2</sup>, Joseph A. Resing<sup>6</sup>, Richard G. Williams<sup>1</sup>

6  
7    <sup>1</sup>School of Environmental Sciences, University of Liverpool, UK

8    <sup>2</sup>School of Ocean and Earth Sciences, University of Southampton, UK

9    <sup>3</sup>University of Leeds, UK

10    <sup>4</sup>Univ Brest, CNRS, Ifremer, IRD, Laboratoire d'Océanographie Physique et Spatiale  
11    (LOPS), IUEM, 29280, Plouzané, France

12    <sup>5</sup>Institut Universitaire de France (IUF), Paris, France

13    <sup>6</sup>University of Washington, USA

14  
15    **Abstract** The dispersal of dissolved iron (DFe) from hydrothermal vents is poorly  
16    constrained. Combining field observations and a hierarchy of models, we show that  
17    the dispersal of DFe from the Trans-Atlantic-Geotraverse vent site occurs  
18    predominantly in the colloidal phase and is controlled by multiple physical processes.  
19    Enhanced mixing near the seafloor and transport through fracture zones at fine-  
20    scales interacts with the wider ocean circulation to drive predominant westward DFe  
21    dispersal away from the Mid-Atlantic ridge at the 100km scale. In contrast, diapycnal  
22    mixing predominantly drives northward DFe transport within the ridge axial valley.  
23    The observed DFe dispersal is not reproduced by the coarse resolution ocean  
24    models typically used to assess ocean iron cycling due to their omission of local  
25    topography and mixing. Unless biogeochemical models include high-resolution  
26    nested grids, they will inaccurately represent DFe dispersal from axial valley ridge  
27    systems, which make up half of the global ocean ridge crest.

28  
29    149/150wds

30  
31    **Plain Language Summary**

32  
33    Hydrothermal venting along mid ocean ridges supplies large quantities of the trace  
34    metal iron to the ocean. Once it mixed with oxygenated seawater, precipitation leads  
35    to iron being lost from the dissolved phase to generate seafloor metal deposits.  
36    However, a small fraction of iron supplied escapes precipitation and remains in the  
37    dissolved phase. The processes that control the retention and ocean transport of  
38    hydrothermal dissolved iron is important as it has a disproportionate influence on the  
39    global carbon cycle. In this work we examined the processes driving the dispersal of  
40    dissolved iron from a major site of hydrothermal venting on the northern mid Atlantic  
41    ridge. We found that the complex topography of the mid Atlantic ridge was crucial in  
42    steering the escape of dissolved iron in the colloidal size range out of the immediate  
43    mid ocean ridge system. This raises challenges for the large scale ocean models  
44    used to represent the global ocean iron cycle as they are typically not parameterised  
45    at high enough spatial resolution. The use of multiple grids, with higher resolution  
46    nests, may offer a solution to the challenge of representing the interactions of tracer  
47    dispersal with complex topography.

48  
49    **Key points:**

- 51 1. Iron is dispersed from TAG predominantly northward within the axial valley and  
52 westward off axis, dominated by the colloidal size fraction  
53 2. A combination of fine-scale processes are necessary to explain the dispersal both  
54 within and outside the axial valley  
55 3. Coarse resolution models are impaired in their ability to constrain the broader  
56 influence of iron supplied from axial valley ridge systems

57  
58

## 59 1. Introduction

60

61 Dissolved iron (DFe) supply from hydrothermal vents has emerged as an important  
62 component of the ocean iron cycle [Tagliabue *et al.*, 2017]. Moreover, as  
63 hydrothermally sourced iron is ventilated in the iron-limited Southern Ocean, there is  
64 an important link to the ocean carbon cycle [Resing *et al.*, 2015; Tagliabue *et al.*,  
65 2010; Tagliabue and Resing, 2016]. Consequently, there is a need to include  
66 hydrothermal DFe supply in ocean biogeochemical models to accurately represent  
67 the supply and cycling of this key micronutrient. Elevated iron signals have been  
68 observed in plumes above most mid ocean ridge systems [Baker *et al.*, 2002; Gamo  
69 *et al.*, 1996; Hahm *et al.*, 2015; Massoth *et al.*, 1994; Rudnicki and Elderfield, 1993].  
70 More recently, as part of the GEOTRACES programme, iron has been shown to  
71 persist as DFe above and beyond the global ridge crest system [Hatta *et al.*, 2015;  
72 Klunder *et al.*, 2011; Nishioka *et al.*, 2013; Resing *et al.*, 2015; Tagliabue *et al.*,  
73 2022]. Crucial in this growing role for hydrothermalism in shaping basin scale  
74 distributions is the question of how DFe is transported away from hydrothermal vent  
75 sites at the >100km scale [Tagliabue and Resing, 2016].

76

77 DFe (<0.2 µm) is an operational definition that encompasses a complex array of  
78 chemical species. In particular, contributions of biogenic and non-biogenic phases  
79 will play an important role in the colloidal size fraction (>0.02µm, but <0.2 µm)  
80 [Tagliabue *et al.*, 2017]. This is particularly true in hydrothermal settings, where large  
81 fluxes of reduced soluble forms of iron interact with oxygenated seawater to drive  
82 rapid changes in physico-chemical speciation [Field and Sherrell, 2000; Rudnicki and  
83 Elderfield, 1993]. In the deep ocean, colloidal and soluble forms of DFe have been  
84 observed to exist in a 1:1 ratio, but closer to iron sources or in the upper ocean the  
85 colloidal contribution can fluctuate notably [Bergquist *et al.*, 2007; Fitzsimmons and  
86 Boyle, 2014; Kunde *et al.*, 2019; Nishioka *et al.*, 2001]. Colloidal iron is typically  
87 made up of iron (oxy)hydroxide phases and small lithogenic particles, as well as  
88 biomolecules and small bacteria or viruses that interact with organics [Lough *et al.*,  
89 2019; Tagliabue *et al.*, 2017].

90

91 The global mid ocean ridge crest displays variable spreading rates and associated  
92 topographic settings, with potential implications for DFe supply and transport. Inert  
93 passive tracers of hydrothermal inputs, like mantle helium-3 ( ${}^3\text{He}$ ), are elevated in  
94 basins with fast spreading ridges, like the Pacific, and depressed where ridge  
95 spreading rates are lower, like the Atlantic [Jenkins *et al.*, 2019]. This is important as  
96 although hydrothermal dFe inputs are parameterised in global models with constant  
97 DFe: ${}^3\text{He}$  ratios following Tagliabue *et al.* [2010], hydrothermal DFe anomalies are  
98 higher than would be expected along the slow spreading mid Atlantic ridge based on  
99  ${}^3\text{He}$  values (e.g. [Hatta *et al.*, 2015; Saito *et al.*, 2013]). Adding further complexity is  
100 the fact that the slow spreading ridges like the mid-Atlantic ridge are typified by large

101 axial valleys with topographic relief varying by kilometres across relatively small  
102 spatial scales. It is not known how resolving these scales of variability affects the  
103 transport of DFe into the wider basin and the implications for coarse resolution ocean  
104 biogeochemical models that are typically used to test hypothesis about hydrothermal  
105 DFe supply and cycling [Roshan *et al.*, 2020; Somes *et al.*, 2021; Tagliabue *et al.*,  
106 2022].

107

108 Here we present new observations of DFe and colloidal Fe from the trans Atlantic  
109 geotraverse (TAG) hydrothermal site northern mid-Atlantic ridge as part of the UK  
110 GEOTRACES GA13 section. Our data document transport of DFe northwards within  
111 the axial valley and westward off axis into the wider basin at a range of spatial  
112 scales. Using a suite of model experiments at a range of resolutions, we diagnose  
113 the candidate physical processes that drive this behaviour and demonstrate that they  
114 are absent in coarse resolution models. This raises important questions about  
115 whether coarse resolution models are appropriate tools to explore iron cycle  
116 pathways associated with DFe supply from slow spreading ridge systems.

117

## 118 **2. Methods**

119

120 The UK GEOTRACES GA13 voyage sailed between Southampton and Guadeloupe  
121 in 2017/8 and as part of the sampling a detailed process study was conducted  
122 around the TAG hydrothermal vent system. A number of stations were sampled  
123 north and south of TAG within the axial valley, as well as east and west off axis into  
124 the Atlantic basin (Figure 1, Supplementary Figure 1). Station spacing ranged from  
125 10-30km close to TAG and up to 100-200km for the farthest stations.

126

127 All sampling protocols followed those established by the GEOTRACES program  
128 [Cutter *et al.*, 2010]. Water samples were collected using Teflon coated Niskin-X  
129 bottles (Ocean Test Equipment) on a kevlar coated conducting wire. Water samples  
130 were filtered (0.2 µm, Sartorius) into acid clean low-density polyethylene bottles for  
131 DFe. A separate aliquot seawater was filtered through 0.02 µm filters (Anotop,  
132 Whatman) for soluble Fe (SFe) (Ussher *et al.*, 2010). All filtration was done in a class  
133 100 clean laboratory on board the ship. Samples were acidified onboard to 0.024 M  
134 (UpA HCl, Romil). Samples were analysed for Fe concentrations using flow injection  
135 chemiluminescence and inductively coupled plasma mass spectrometry. In both  
136 cases GEOTRACES reference materials (D2, GSC, GSP) were analysed and there  
137 was a maximum difference of 0.14 nM between measured and consensus values  
138 (Measured GSC  $2.04 \pm 0.03$  nM, consensus GSC  $2.18 \pm 0.08$  nM). For further  
139 details see [Lough *et al.*, 2022].

140

141 Two Lagrangian dispersion experiments were carried out using the 3D velocity  
142 field of the GIGATL3 simulation. GIGATL3 is a regional simulation of the  
143 ocean physical state in the Atlantic Ocean based on the primitive-equation  
144 CROCO model, developed using the Regional Oceanic Modeling System  
145 [Shchepetkin and McWilliams, 2005]. The GIGATL3 simulation has a nominal  
146 horizontal resolution of 3 km and features 100 terrain-following vertical levels, with  
147 stretching near the surface and seafloor (supplementary figure 2). The  
148 GIGATL3 bathymetry is taken from the global 30 arc second SRTM30plus data set  
149 [Becker *et al.*, 2009]. The initial state and lateral boundary conditions for velocity, sea  
150 surface height, temperature, and salinity are supplied by the Simple Ocean Data

151 Assimilation data set [Carton and Giese, 2008]. Atmospheric forcing was supplied at  
152 hourly resolution by the Climate Forecast System Reanalysis [Saha et al., 2010].  
153 Tidal forcing derived from TPXO7 is included. The 3D velocity field is saved hourly  
154 and linearly interpolated in space and time to perform two Lagrangian experiments  
155 using the Pyticles software [Gula et al., 2014]. We used these two experiments to  
156 improve the robustness of the dispersion patterns and diagnostics are calculated  
157 using all particles across both experiments. The two experiments are strictly  
158 identical in terms of the particle seeding set up and integration time, only differing by  
159 starting point. The first experiment starts on 2008-08-29 whereas the second starts  
160 on 2010-06-05. Each experiment consists of releasing 25 particles every 6 h at the  
161 TAG vent site plume depth for 8 months. Diagnostics on particle spreading were  
162 performed for particles with ages between 10 and 180 days. As particles are  
163 continuously released, approximately 22000, 14000 or 5800 particles have an overall  
164 lifespan of 10, 90 or 180 days, respectively, for each experiment.  
165

166 Modelling experiments are also conducted using a global scale ocean general  
167 circulation model. We conducted passive release experiments using two  
168 configurations of the Nucleus for European Modelling of the Ocean (NEMO) model.  
169 The first was the standard global configuration using the ORCA2 configuration at a  
170 horizontal resolution of  $2^\circ \times \cos(\text{latitude})$  curvilinear grid, with an enhancement to  
171  $0.5^\circ$  around the equator and 31 irregularly spaced vertical levels. This NEMO-  
172 ORCA2 configuration is typical of those models coupled to biogeochemical models  
173 to address questions regarding biogeochemical cycling (e.g. Tagliabue et al., 2022).  
174 We applied the default settings and boundary conditions of the reference  
175 configuration ORCA2\_ICE\_PISCES [NEMO-Consortium, 2019]. NEMO-ORCA2 is  
176 forced with CORE-II normal year atmospheric forcing, with the NCAR bulk formulae  
177 [Large and Yeager, 2008]. After the initial spin-up, we conducted an idealised  
178 passive tracer release. The passive tracer concentration is continuously set to one at  
179 the deepest grid cell closest to the TAG site. The passive tracer fluxes at the surface,  
180 at the lateral boundaries and at the bottom are set to zero and the surface passive  
181 tracer concentration is restored to zero. The model is run for another 30 years (year  
182 130 to 160) and the tracer spread is monitored. This scenario is repeated with a  
183 NEMO-AGRIF configuration with the addition of two nested regions, covering the  
184 TAG site, via adaptive mesh refinement package [Debreu et al., 2008]. Two level,  
185 two-way nesting is used: the first level covers a region in the subtropical North  
186 Atlantic (dashed rectangle in supplementary figure 3) with refinement ratio of 4 in  
187 both latitude and longitude (to give a horizontal resolution of  $1/2^\circ$ ). The second level  
188 of nesting is applied over a region with the TAG site in the centre, with further  
189 refinement ratio of 4 (solid line rectangle in supplementary figure 3) reaching a  
190 horizontal resolution of  $1/8^\circ$  or 12.48km. The passive tracer is released only in this  
191 high-resolution region. The model bathymetry of the two nested regions is  
192 constructed from the 5 arc minute resolution global bathymetry from ETOPO5. The  
193 initial conditions and the surface forcing functions of the nested regions in NEMO-  
194 AGRIF are interpolated from NEMO-ORCA2 fields using the NEMO nesting tools.  
195

### 196 3. Results

#### 197 3.1 Dispersion of DFe from the TAG hydrothermal vent field

200 The TAG site is a well-studied hydrothermal vent system, sited within the mid-  
201 Atlantic ridge axial valley (Figure 1). As part of the GA03 GEOTRACES section, DFe  
202 measurements were taken at TAG, but the station spacing for full-depth profiles  
203 exceeded 500km [Hatta et al., 2015]. Within the axial valley DFe is predominantly  
204 dispersed northwards in the colloidal phase. The hydrothermal DFe anomaly of  
205 around 80 nM we observed at TAG matches that observed during the GA03 voyage  
206 [Hatta et al., 2015] and persists at 3-4 nM at the stations 19 and 30km north (Figure  
207 1). In contrast, DFe drops below concentrations of 2 nM for the station 30km south,  
208 indicating greater dilution and/or removal from the dissolved phase (Figure 1). At  
209 TAG, the highest concentrations of DFe are associated with very low soluble Fe  
210 fraction (<10%), indicating the dominance of colloidal Fe. At the depths of the  
211 greatest hydrothermal DFe signals, the soluble dFe fraction within the axial valley  
212 also remains low (<25%) within 30km of TAG, again indicating dominance of Fe  
213 colloids in the hydrothermal DFe signal throughout the valley.  
214

215 There is a contrasting DFe signal east and west from TAG off axis from the mid-  
216 Atlantic ridge. At the largest spatial scales, strong hydrothermal DFe anomalies  
217 persist 140-250km west of TAG (stations 28 and 29), but are absent at stations 140-  
218 250km to the east (stations 33 and 32). A marked dFe anomaly between 2,200-  
219 3,400m (centered on 3000m) of 2.64nM 140km from TAG (station 29) declines to a  
220 more localised anomaly of 0.95nM 250km west of TAG (station 28). Both of these  
221 DFe signals are above the concentrations observed at this depth and latitude at the  
222 eastern stations. Notably, the elevated DFe concentrations 140-250km west of TAG  
223 remain associated with low soluble DFe fractions, indicating the importance of Fe  
224 colloids. Consistent with the absence of hydrothermal DFe input or transport, the  
225 soluble iron fraction 140-250km to the east is closer to the 50% typically observed in  
226 the deep ocean [Kunde et al., 2019].  
227

### 228 **3.2 Processes shaping the dispersion from TAG over different space and time 229 scales**

230 The particle release experiments conducted with the high-resolution particle tracking  
231 model reveal the role of different processes shaping dispersion from TAG over  
232 different space and timescales (Figure 2). We particularly note three stages of  
233 physical dispersal.  
234

235 *10-30 days:* In the immediate period following their release, particles preferentially  
236 spread within the axial valley in a northeast-southwest direction, largely under  
237 topographic control (Figure 2ab). The impact of topography is illustrated by the  
238 topostrophy parameter,  $\tau$  [Holloway, 2008], which is elevated and positive within the  
239 valley and much reduced off axis (Supplementary Figure 4). That  $\tau$  is >0 indicates a  
240 cyclonic circulation within the axial valley basins, consistent with observed and  
241 modelled circulations within the MAR valley [Lahaye et al., 2019]. The topography of  
242 the mid Atlantic ridge axial valley also allows particles to rapidly escape the axial  
243 valley along isopycnal surfaces to the southwest via fracture zones within only a few  
244 days (Figure 2a).  
245

246 *60-90 days:* Particles that escape the valley spread isotropically along density  
247 surfaces (Figures 2c,d). The topographic control is now very weak on average as  
248 topographic slopes are weaker and particles are now well above the seafloor  
249

250 (Supplementary Figure 4). Consequently, particles spread mostly along isopycnals  
251 due to the lesser influence of diapycnal mixing processes that were occurring on and  
252 within the axial valley system.

253  
254 120-180 days: After 4-6 months, particles preferentially spread westward outside the  
255 axial valley (Figure 2ef) due to the combination of the large-scale mean sub-tropical  
256 gyre circulation and the planetary beta effect that constrains mesoscale vortices to  
257 travel westward [Killworth, 1983; Nof, 1981]. By this stage, transport within the axial  
258 valley also demonstrates a predominantly northward signal as particles fill the  
259 northern axial valley basin within the mid-Atlantic ridge north of TAG. Notably,  
260 dispersal westward off axis into the wider Atlantic Ocean basin and northward within  
261 the axial valley matches the observed DFe concentration anomalies closely (Figure  
262 1), as well as understanding from prior work [Thurnherr et al., 2002; Vic et al., 2018;  
263 Yearsley et al., 2020].

264  
265 **3.3 The importance of bottom topography in representing hydrothermal Fe  
266 supply in global ocean models**

267  
268 The set of simulations conducted with two NEMO allow us to explore how the  
269 dispersion of hydrothermal tracers from TAG are represented by coarse resolution  
270 NEMO-ORCA2 global models and with the NEMO-AGRIF configuration. The NEMO-  
271 AGRIF configuration has a 1/8° (or 12.48km) resolution regional nested grid around  
272 TAG (supplementary figure 3), but the vertical resolution of NEMO-AGRIF and  
273 NEMO-ORCA2 are around three-fold lower than the particle tracking model. This set  
274 of model configurations were designed to link the very high-resolution regional  
275 modelling with the types of models used for larger scale biogeochemical modelling  
276 that tend to have horizontal resolutions of between 1-5° [Roshan et al., 2020; Somes  
277 et al., 2021; Tagliabue et al., 2022].

278  
279 In general, the NEMO-AGRIF model shows very similar dispersal patterns to the  
280 high-resolution particle model, with strong signals remaining localised within the axial  
281 valley and spreading preferentially north within the axial valley and westward off-axis  
282 (Figure 3). In contrast, the NEMO-ORCA2 configuration typically used for  
283 assessments of iron biogeochemistry show two major deficiencies, relative to the  
284 nested NEMO-AGRIF and high-resolution particle models (Figure 2), as well as the  
285 observations (Figure 1). First, high concentrations of tracer do not remain trapped in  
286 the ridge system. Second, large scale dispersal operates equally away from the  
287 ridge both east and west, rather than predominantly to the west. These deficiencies  
288 in the zonal dispersal can be illustrated by a section taken along 26N, with the  
289 NEMO-AGRIF nested model displaying dispersal was (i) more restricted and (ii)  
290 predominantly westward as compared to the coarse resolution NEMO-ORCA2  
291 model. Notably, both NEMO-ORCA2 and NEMO-AGRIF share the same number  
292 and arrangement of vertical levels, highlighting the importance of the horizontal  
293 resolution in improving the agreement with both high-resolution particle tracking  
294 models and inferences regarding dispersal gleaned from direct observations of DFe.  
295 To compare the model configurations more directly against observations we merged  
296 the GA13 data from this study with DFe observations from the GA03 GEOTRACES  
297 section that followed the same cruise track, which displays a similar westward  
298 propagation off axis from TAG (Figure 3e).

300 **4. Discussion**

301

302 **4.1 Processes driving the dispersal of iron from the mid-Atlantic ridge**

303

304 Dispersal of DFe from TAG is controlled by a combination of local mixing across  
305 density surfaces and the specific geometry of the mid Atlantic ridge. Using our  
306 particle tracking simulations, we tracked the cumulative changes in density during  
307 the particle lifetimes to identify the importance of across isopycnal mixing in  
308 explaining whether DFe dispersal west of TAG (Figure 3e) is over or around  
309 topography. Enhanced mixing is associated with small scale internal tides and  
310 mesoscale currents interacting with topographic features, such as mid ocean ridges  
311 [Vic *et al.*, 2019]. The average cumulative change in density across all particles  
312 highlights strong transfer to lighter density surfaces on the ridge crest and within the  
313 axial valley (Figure 4a). Small average changes outside the axial valley are  
314 associated with large variability (Figure 4b). Focussing on an example site outside  
315 the valley, we can see that while average cumulative density changes are close to  
316 zero, 64% of all particles experience lightening (Figure 4c, Supplementary Figure 5),  
317 leading to around 200m elevation in absolute depth (Figure 4d). Within the valley,  
318 the change in cumulative density is much more striking (Figure 4c), with changes in  
319 absolute elevation of closer to 100m (Figure 4d). The larger changes in absolute  
320 depth, despite smaller changes in cumulative density outside the valley are  
321 associated with slumping and heaving of isopycnal layers. Overall, the significant  
322 population of particles outside the valley without strong cumulative density changes  
323 demonstrates the transfer of particles through fracture zones and highlights the role  
324 of local geometry of the mid Atlantic ridge system (see Sec 3.2 and 3.3,  
325 Supplementary Figure 5). Within the valley, across density mixing associated with  
326 topography is much more important.

327

328 By examining the lifetime of particles reaching the local particle maxima at any given  
329 location, we can quantify timescales of dispersion across the two Lagrangian  
330 experiments (Figure 4e). Dispersion from TAG takes at least 100 days to reach  
331 140km west of TAG (station 29) or exceeds 150 days to reach station 28 at 250km  
332 from TAG (Figure 4). Since most hydrothermal iron is associated with maxima in  
333 colloidal Fe, this indicates relatively strong stability of colloidal iron phases during  
334 transport (for at least 6 months). We note that these estimates should be seen as  
335 minimum estimates for transport to the different locations. If we integrated the  
336 particle model longer, we would potentially also observe the arrival of older particles  
337 and find evidence for longer term stability of colloidal iron. The extended lifetime of  
338 colloidal iron may be driven by slower oxidation of colloidal iron [Gartman and  
339 Luther, 2014] or its association with organic phases [Fitzsimmons *et al.*, 2017].

340

341 **4.2 Using model-observation studies to quantify iron cycle mechanisms**

342

343 Combining global ocean biogeochemical modelling experiments with GEOTRACES  
344 datasets have played a key role in identifying significant processes shaping the  
345 ocean iron cycle and their wider impacts. However, their results may be  
346 compromised when the model resolution is insufficient for the system of interest. Our  
347 results show that only model experiments at the 10s of km horizontal resolution can  
348 accurately represent the dispersal of DFe from the TAG site on the mid-Atlantic  
349 ridge, far exceeding the typical resolution of global ocean biogeochemical models

350 (100-500km). This is due to the complex topography of the axial valley setting of the  
351 TAG site that is not resolved in global ocean biogeochemical models. Where ridge  
352 topography is less variable, for instance at faster ridge spreading sites, e.g. the East  
353 Pacific Rise, coarser resolutions may be sufficient [Resing et al., 2015]. Our results  
354 suggest that new solutions, accounting for high-resolution sub grids, are required to  
355 properly represent DFe dispersal at scales exceeding 100km from the axial valley  
356 settings that make up around half of the mid ocean ridge crest. Improved vertical  
357 resolution may also be important, but this was not assessed directly in this study as  
358 both NEMO model configurations had the same number and arrangement of vertical  
359 levels.

360

361 The role of representing DFe input and wider transport around local topography in  
362 coarse resolution models may be more generically relevant. For instance, continental  
363 shelves can also be associated with complex topographic geometry and coarse  
364 resolution models may face similar challenges in properly representing the dispersal  
365 of tracers supplied, such as DFe. For instance, in the North Pacific, the DFe inputs  
366 from sediment resuspension disperses from the sea of Okhotsk into the wider North  
367 Pacific basin via North Pacific Intermediate Water (NPIW) [Nishioka et al., 2021;  
368 Nishioka et al., 2020]. An important component of this dispersal is the strong  
369 topographically induced diapycnal mixing that occurs over the Kuril straits [Yagi and  
370 Yasuda, 2012], transporting DFe onto the NPIW isopycnals to then spread  
371 throughout the North Pacific basin [Nishioka et al., 2020]. Tidal mixing along the  
372 shelf break may also be an important component of DFe supply in the southern  
373 Bering Sea [Tanaka et al., 2012], as well as seamounts [Lavelle et al., 2004].  
374 Therefore, it is important to consider any biases in the DFe dispersal from both  
375 hydrothermal and sediment inputs that may arise from insufficient resolution in  
376 process-based models.

377

## 378 5. Conclusions

379

380 Using a novel sampling strategy at a scale of 10s and 100s of km around the TAG  
381 vent site, we document the predominant transport pathways of hydrothermal DFe.  
382 Our observations indicated DFe was transported northward within the axial valley  
383 and westward off axis in the colloidal size fraction. Dispersal within the valley arose  
384 due to the diapycnal mixing that resulted from topographic interaction. Transport off  
385 axis resulted from both diapycnal mixing and the fine scales of axial valley geometry,  
386 especially fracture zones. The dispersal patterns of DFe were reproduced with a  
387 high-resolution particle tracking model and a global model with a nested ~10km  
388 horizontal grid, but not with a global ocean configuration. This raises challenges for  
389 correctly representing DFe supply and the associated biogeochemical impacts from  
390 axial valley hydrothermal vent systems, as well as other supply mechanisms around  
391 local topographical features.

392

## 393 6. Acknowledgements

394

395 This work is part of the United Kingdom GEOTRACES section GA13 which was  
396 supported by the Natural Environment Research Council (NERC) Grants  
397 NE/N009525/1 to AT and NE/N010396/1 to MCL. We thank the Captain and crew of  
398 the *RRS James Cook* and everyone that contributed to the GA13 sampling effort on  
399 board. JG acknowledges support from the French National Agency for Research

400 (ANR) through the project DEEPER (ANR-19- CE01-0002-01), and PRACE and  
401 GENCI for awarding access to HPC resources Joliot-Curie Rome and SKL from  
402 GENCI-TGCC (grants 2020-A0090112051, 2019gch0401, and PRACE project  
403 2018194735) and HPC facilities DATARMOR of “Pôle de Calcul Intensif pour la Mer”  
404 at Ifremer Brest France. The authors thank Gildas Cambon and Sébastien Theetten  
405 for their contribution in the development of the GIGATL3 simulation. JAR was funded  
406 by NOAA Ocean Exploration and Earth Ocean Interactions program; this is PMEL  
407 #XXX and CICOES publication # YYYY. The International GEOTRACES Programme  
408 is possible in part thanks to the support from the U.S. National Science Foundation  
409 (Grant OCE-1840868) to the Scientific Committee on Oceanic Research (SCOR).  
410

#### 411 **Data availability statement:**

412  
413 CROCO ocean model is available at <https://www.croc-ocean.org>. Information about  
414 the GIGATL6 simulation can be found at <https://doi.org/10.5281/zenodo.4948523>  
415  
416 The Lagrangian software Pyticles is available  
417 at <https://github.com/Mesharou/Pyticles> and has been archived on Zenodo  
418 at <https://doi.org/10.5281/zenodo.4973786>.  
419

420 The data from the GA13 transect is available (to view and download) as part of the  
421 GEOTRACES intermediate data product 2021 which can be accessed online via  
422 <https://www.geotraces.org/geotraces-intermediate-data-product-2021/>  
423

## 424 **7. References**

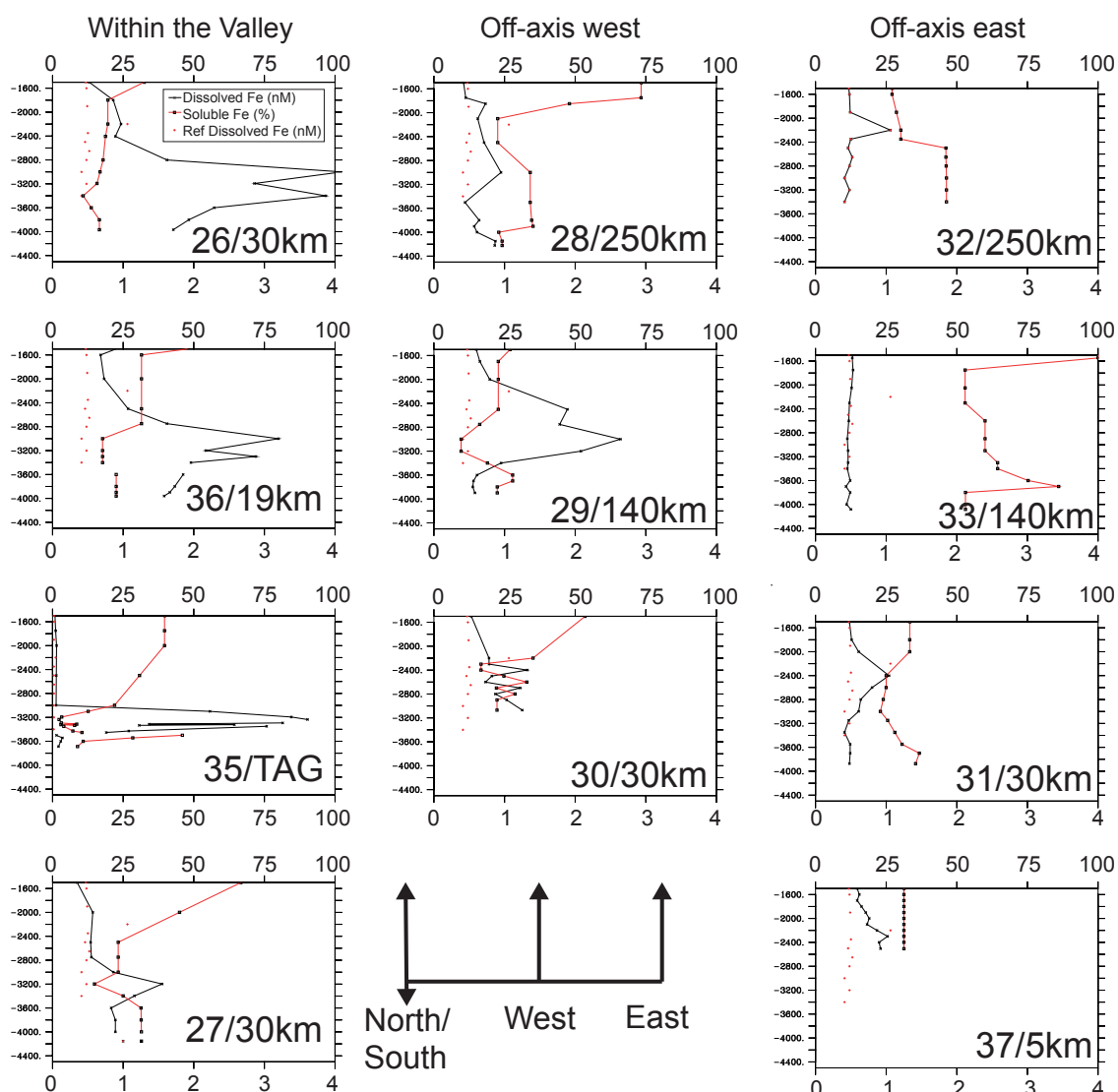
- 425  
426 Baker, E. T., et al. (2002), Hydrothermal venting along Earth's fastest spreading  
427 center: East Pacific Rise, 27.5°–32.3°, *Journal of Geophysical Research: Solid Earth*,  
428 107(B7), EPM 2-1-EPM 2-14, doi:10.1029/2001jb000651.  
429 Becker, J. J., et al. (2009), Global Bathymetry and Elevation Data at 30 Arc Seconds  
430 Resolution: SRTM30\_PLUS, *Marine Geodesy*, 32(4), 355-371,  
431 doi:10.1080/01490410903297766.  
432 Bergquist, B. A., J. Wu, and E. A. Boyle (2007), Variability in oceanic dissolved iron  
433 is dominated by the colloidal fraction, *Geochimica et Cosmochimica Acta*, 71(12),  
434 2960-2974, doi:10.1016/j.gca.2007.03.013.  
435 Carton, J. A., and B. S. Giese (2008), A Reanalysis of Ocean Climate Using Simple  
436 Ocean Data Assimilation (SODA), *Monthly Weather Review*, 136(8), 2999-3017,  
437 doi:10.1175/2007mwr1978.1.  
438 Cutter, G., P. Andersson, L. Codispoti, P. Croot, R. François, M. C. Lohan, H. Obata,  
439 and M. Rutgers v. d. Loeff (2010), Sampling and Sample-handling Protocols for  
440 GEOTRACES Cruises, edited, doi:<https://epic.awi.de/id/eprint/34484>.  
441 Debreu, L., C. Voulard, and E. Blayo (2008), AGRIF: Adaptive grid refinement in  
442 Fortran, *Computers & Geosciences*, 34(1), 8-13, doi:10.1016/j.cageo.2007.01.009.

- 443 Field, M. P., and R. M. Sherrell (2000), Dissolved and particulate Fe in a  
444 hydrothermal plume at 9°45'N, East Pacific Rise, *Geochimica et Cosmochimica  
445 Acta*, 64(4), 619-628, doi:10.1016/s0016-7037(99)00333-6.
- 446 Fitzsimmons, J. N., and E. A. Boyle (2014), Both soluble and colloidal iron phases  
447 control dissolved iron variability in the tropical North Atlantic Ocean, *Geochimica et  
448 Cosmochimica Acta*, 125, 539-550, doi:10.1016/j.gca.2013.10.032.
- 449 Fitzsimmons, J. N., S. G. John, C. M. Marsay, C. L. Hoffman, Sarah L. Nicholas, B.  
450 M. Toner, C. R. German, and R. M. Sherrell (2017), Iron persistence in a distal  
451 hydrothermal plume supported by dissolved–particulate exchange, *Nature  
452 Geoscience*, 10(3), 195-201, doi:10.1038/ngeo2900.
- 453 Gamo, T., et al. (1996), Hydrothermal plumes at the Rodriguez triple junction, Indian  
454 ridge, *Earth and Planetary Science Letters*, 142(1-2), 261-270, doi:10.1016/0012-  
455 821x(96)00087-8.
- 456 Gartman, A., and G. W. Luther (2014), Oxidation of synthesized sub-micron pyrite  
457 (FeS<sub>2</sub>) in seawater, *Geochimica et Cosmochimica Acta*, 144, 96-108,  
458 doi:10.1016/j.gca.2014.08.022.
- 459 Gula, J., M. J. Molemaker, and J. C. McWilliams (2014), Submesoscale cold  
460 filaments in the Gulf Stream, *Journal of Physical Oceanography*, 44(10), 2617-2643,  
461 doi:10.1175/JPO-D-14-0029.1s.
- 462 Hahm, D., E. T. Baker, T. Siek Rhee, Y.-J. Won, J. A. Resing, J. E. Lupton, W.-K.  
463 Lee, M. Kim, and S.-H. Park (2015), First hydrothermal discoveries on the  
464 Australian-Antarctic Ridge: Discharge sites, plume chemistry, and vent organisms,  
465 *Geochemistry, Geophysics, Geosystems*, 16(9), 3061-3075,  
466 doi:10.1002/2015gc005926.
- 467 Hatta, M., C. I. Measures, J. Wu, S. Roshan, J. N. Fitzsimmons, P. Sedwick, and P.  
468 Morton (2015), An overview of dissolved Fe and Mn distributions during the 2010–  
469 2011 U.S. GEOTRACES north Atlantic cruises: GEOTRACES GA03, *Deep Sea  
470 Research Part II: Topical Studies in Oceanography*, 116, 117-129,  
471 doi:10.1016/j.dsr2.2014.07.005.
- 472 Holloway, G. (2008), Observing global ocean topostrophy, *Journal of Geophysical  
473 Research*, 113(C7), doi:10.1029/2007jc004635.
- 474 Jenkins, W. J., et al. (2019), A comprehensive global oceanic dataset of helium  
475 isotope and tritium measurements, *Earth System Science Data*, 11(2), 441-454,  
476 doi:10.5194/essd-11-441-2019.
- 477 Killworth, P. D. (1983), On the Motion of Isolated Lenses on a Beta-Plane, *Journal of  
478 Physical Oceanography*, 13(3), 368-376, doi:10.1175/1520-  
479 0485(1983)013<0368:Otmoil>2.0.Co;2.
- 480 Klunder, M. B., P. Laan, R. Middag, H. J. W. De Baar, and J. C. van Ooijen (2011),  
481 Dissolved iron in the Southern Ocean (Atlantic sector), *Deep Sea Research Part II:  
482 Topical Studies in Oceanography*, 58(25-26), 2678-2694,  
483 doi:10.1016/j.dsr2.2010.10.042.

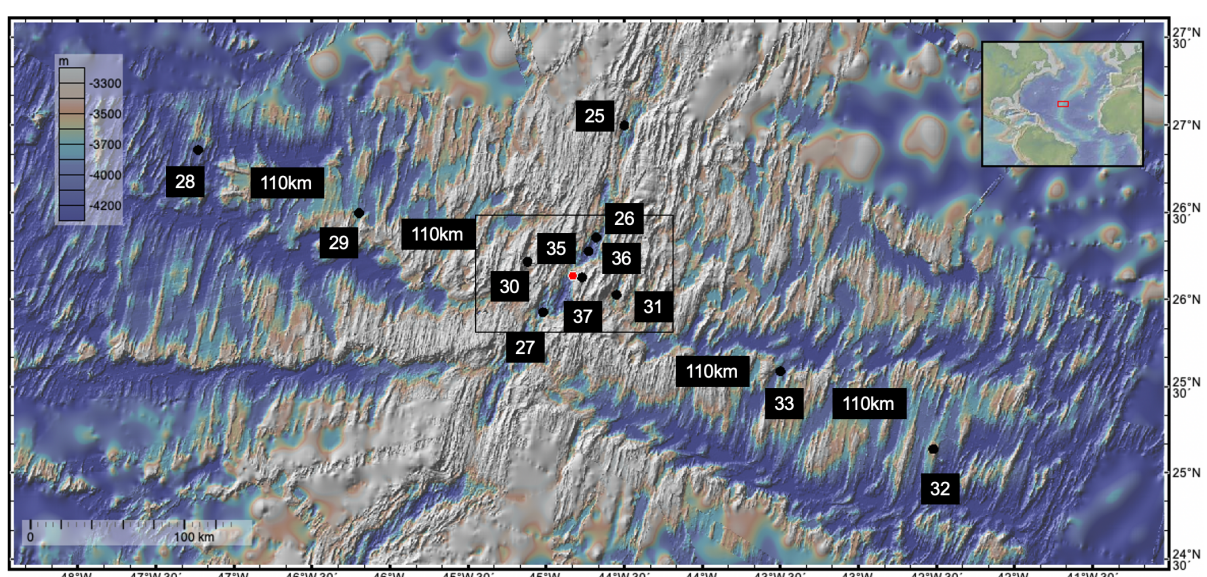
- 484 Kunde, K., N. J. Wyatt, D. González-Santana, A. Tagliabue, C. Mahaffey, and M. C.  
485 Lohan (2019), Iron Distribution in the Subtropical North Atlantic: The Pivotal Role of  
486 Colloidal Iron, *Global Biogeochemical Cycles*, 33(12), 1532-1547,  
487 doi:10.1029/2019gb006326.
- 488 Lahaye, N., J. Gula, A. M. Thurnherr, G. Reverdin, P. Bouruet-Aubertot, and G.  
489 Roullet (2019), Deep Currents in the Rift Valley of the North Mid-Atlantic Ridge,  
490 *Frontiers in Marine Science*, 6, doi:10.3389/fmars.2019.00597.
- 491 Large, W. G., and S. G. Yeager (2008), The global climatology of an interannually  
492 varying air-sea flux data set, *Climate Dynamics*, 33(2-3), 341-364,  
493 doi:10.1007/s00382-008-0441-3.
- 494 Lavelle, J. W., I. D. Lozovatsky, and D. C. Smith (2004), Tidally induced turbulent  
495 mixing at Irving Seamount-Modeling and measurements, *Geophysical Research  
Letters*, 31(10), n/a-n/a, doi:10.1029/2004gl019706.
- 497 Lough, A. J. M., W. B. Homoky, D. P. Connelly, S. A. Comer-Warner, K. Nakamura,  
498 M. K. Abyaneh, B. Kaulich, and R. A. Mills (2019), Soluble iron conservation and  
499 colloidal iron dynamics in a hydrothermal plume, *Chemical Geology*, 511, 225-237,  
500 doi:10.1016/j.chemgeo.2019.01.001.
- 501 Lough, A. J. M., A. Tagliabue, C. Demasy, J. A. Resing, T. Mellett, N. J. Wyatt, and  
502 M. C. Lohan (2022), The impact of hydrothermal vent geochemistry on the addition  
503 of iron to the deep ocean, *Biogeosciences Discussions*, [preprint], doi:10.5194/bg-  
504 2022-73.
- 505 Massoth, G. J., E. T. Baker, J. E. Lupton, R. A. Feely, D. A. Butterfield, K. L. Von  
506 Damm, K. K. Roe, and G. T. Lebon (1994), Temporal and spatial variability of  
507 hydrothermal manganese and iron at Cleft segment, Juan de Fuca Ridge, *Journal of  
508 Geophysical Research: Solid Earth*, 99(B3), 4905-4923, doi:10.1029/93jb02799.
- 509 NEMO-Consortium (2019), NEMO Reference configurations inputs (v4.0.1),  
510 doi:10.5281/zenodo.1471701.
- 511 Nishioka, J., H. Obata, T. Hirawake, Y. Kondo, Y. Yamashita, K. Misumi, and I.  
512 Yasuda (2021), A review: iron and nutrient supply in the subarctic Pacific and its  
513 impact on phytoplankton production, *Journal of Oceanography*, 77(4), 561-587,  
514 doi:10.1007/s10872-021-00606-5.
- 515 Nishioka, J., H. Obata, H. Ogawa, K. Ono, Y. Yamashita, K. Lee, S. Takeda, and I.  
516 Yasuda (2020), Subpolar marginal seas fuel the North Pacific through the  
517 intermediate water at the termination of the global ocean circulation, *Proceedings of  
518 the National Academy of Sciences*, 117(23), 12665-12673,  
519 doi:doi:10.1073/pnas.2000658117.
- 520 Nishioka, J., H. Obata, and D. Tsumune (2013), Evidence of an extensive spread of  
521 hydrothermal dissolved iron in the Indian Ocean, *Earth and Planetary Science  
Letters*, 361, 26-33, doi:10.1016/j.epsl.2012.11.040.

- 523 Nishioka, J., S. Takeda, C. S. Wong, and W. K. Johnson (2001), Size-fractionated  
524 iron concentrations in the northeast Pacific Ocean: distribution of soluble and small  
525 colloidal iron, *Marine Chemistry*, 74(2-3), 157-179, doi:10.1016/s0304-  
526 4203(01)00013-5.
- 527 Nof, D. (1981), On the  $\beta$ -Induced Movement of Isolated Baroclinic Eddies, *Journal of*  
528 *Physical Oceanography*, 11(12), 1662-1672, doi:10.1175/1520-  
529 0485(1981)011<1662:Otimoi>2.0.Co;2.
- 530 Resing, J. A., P. N. Sedwick, C. R. German, W. J. Jenkins, J. W. Moffett, B. M.  
531 Sohst, and A. Tagliabue (2015), Basin-scale transport of hydrothermal dissolved  
532 metals across the South Pacific Ocean, *Nature*, 523(7559), 200-203,  
533 doi:10.1038/nature14577.
- 534 Roshan, S., T. DeVries, J. Wu, S. John, and T. Weber (2020), Reversible  
535 scavenging traps hydrothermal iron in the deep ocean, *Earth and Planetary Science*  
536 *Letters*, 542, doi:10.1016/j.epsl.2020.116297.
- 537 Rudnicki, M. D., and H. Elderfield (1993), A chemical model of the buoyant and  
538 neutrally buoyant plume above the TAG vent field, 26 degrees N, Mid-Atlantic Ridge,  
539 *Geochimica et Cosmochimica Acta*, 57(13), 2939-2957, doi:10.1016/0016-  
540 7037(93)90285-5.
- 541 Saha, S., et al. (2010), The NCEP Climate Forecast System Reanalysis, *Bulletin of*  
542 *the American Meteorological Society*, 91(8), 1015-1058,  
543 doi:10.1175/2010bams3001.1.
- 544 Saito, M. A., A. E. Noble, A. Tagliabue, T. J. Goepfert, C. H. Lamborg, and W. J.  
545 Jenkins (2013), Slow-spreading submarine ridges in the South Atlantic as a  
546 significant oceanic iron source, *Nature Geoscience*, 6(9), 775-779,  
547 doi:10.1038/Ngeo1893.
- 548 Shchepetkin, A. F., and J. C. McWilliams (2005), The regional oceanic modeling  
549 system (ROMS): a split-explicit, free-surface, topography-following-coordinate  
550 oceanic model, *Ocean Modelling*, 9(4), 347-404, doi:10.1016/j.ocemod.2004.08.002.
- 551 Somes, C. J., A. W. Dale, K. Wallmann, F. Scholz, W. Yao, A. Oschlies, J. Muglia, A.  
552 Schmittner, and E. P. Achterberg (2021), Constraining Global Marine Iron Sources  
553 and Ligand-Mediated Scavenging Fluxes With GEOTRACES Dissolved Iron  
554 Measurements in an Ocean Biogeochemical Model, *Global Biogeochemical Cycles*,  
555 35(8), doi:10.1029/2021gb006948.
- 556 Tagliabue, A., et al. (2010), Hydrothermal contribution to the oceanic dissolved iron  
557 inventory, *Nature Geoscience*, 3(4), 252-256, doi:10.1038/ngeo818.
- 558 Tagliabue, A., A. R. Bowie, P. W. Boyd, K. N. Buck, K. S. Johnson, and M. A. Saito  
559 (2017), The integral role of iron in ocean biogeochemistry, *Nature*, 543(7643), 51-59,  
560 doi:10.1038/nature21058.
- 561 Tagliabue, A., A. R. Bowie, T. Holmes, P. Latour, P. van der Merwe, M. Gault-  
562 Ringold, K. Wuttig, and J. A. Resing (2022), Constraining the Contribution of

- 563 Hydrothermal Iron to Southern Ocean Export Production Using Deep Ocean Iron  
564 Observations, *Frontiers in Marine Science*, 9, doi:10.3389/fmars.2022.754517.
- 565 Tagliabue, A., and J. Resing (2016), Impact of hydrothermalism on the ocean iron  
566 cycle, *Philosophical transactions. Series A, Mathematical, physical, and engineering*  
567 *sciences*, 374(2081), doi:10.1098/rsta.2015.0291.
- 568 Tanaka, T., I. Yasuda, K. Kuma, and J. Nishioka (2012), Vertical turbulent iron flux  
569 sustains the Green Belt along the shelf break in the southeastern Bering Sea,  
570 *Geophysical Research Letters*, 39(8), n/a-n/a, doi:10.1029/2012gl051164.
- 571 Thurnherr, A. M., K. J. Richards, C. R. German, G. F. Lane-Serff, and K. G. Speer  
572 (2002), Flow and Mixing in the Rift Valley of the Mid-Atlantic Ridge, *Journal of*  
573 *Physical Oceanography*, 32(6), 1763-1778, doi:10.1175/1520-  
574 0485(2002)032<1763:Famitr>2.0.Co;2.
- 575 Vic, C., J. Gula, G. Roullet, and F. Pradillon (2018), Dispersion of deep-sea  
576 hydrothermal vent effluents and larvae by submesoscale and tidal currents, *Deep*  
577 *Sea Research Part I: Oceanographic Research Papers*, 133, 1-18,  
578 doi:10.1016/j.dsr.2018.01.001.
- 579 Vic, C., A. C. Naveira Garabato, J. A. M. Green, A. F. Waterhouse, Z. Zhao, A.  
580 Melet, C. de Lavergne, M. C. Buijsman, and G. R. Stephenson (2019), Deep-ocean  
581 mixing driven by small-scale internal tides, *Nature communications*, 10(1), 2099,  
582 doi:10.1038/s41467-019-10149-5.
- 583 Yagi, M., and I. Yasuda (2012), Deep intense vertical mixing in the Bussol' Strait,  
584 *Geophysical Research Letters*, 39(1), n/a-n/a, doi:10.1029/2011gl050349.
- 585 Yearsley, J. M., D. M. Salmanidou, J. Carlsson, D. Burns, and C. L. Van Dover  
586 (2020), Biophysical models of persistent connectivity and barriers on the northern  
587 Mid-Atlantic Ridge, *Deep Sea Research Part II: Topical Studies in Oceanography*,  
588 180, doi:10.1016/j.dsr2.2020.104819.
- 589  
590

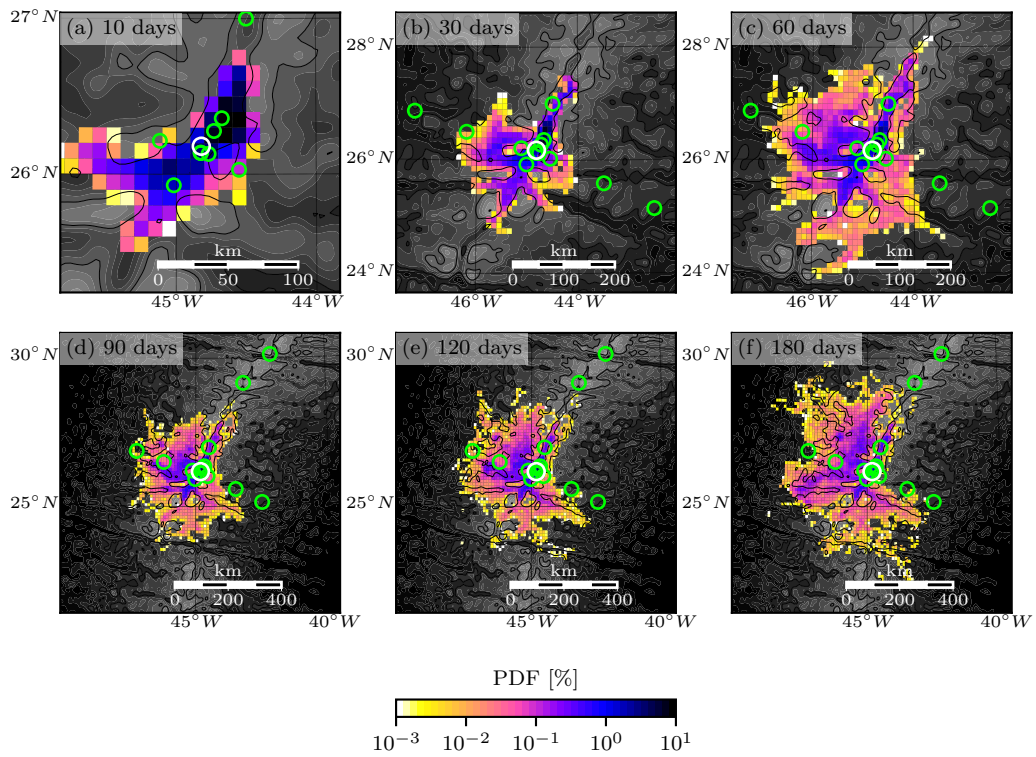
591  
592

593

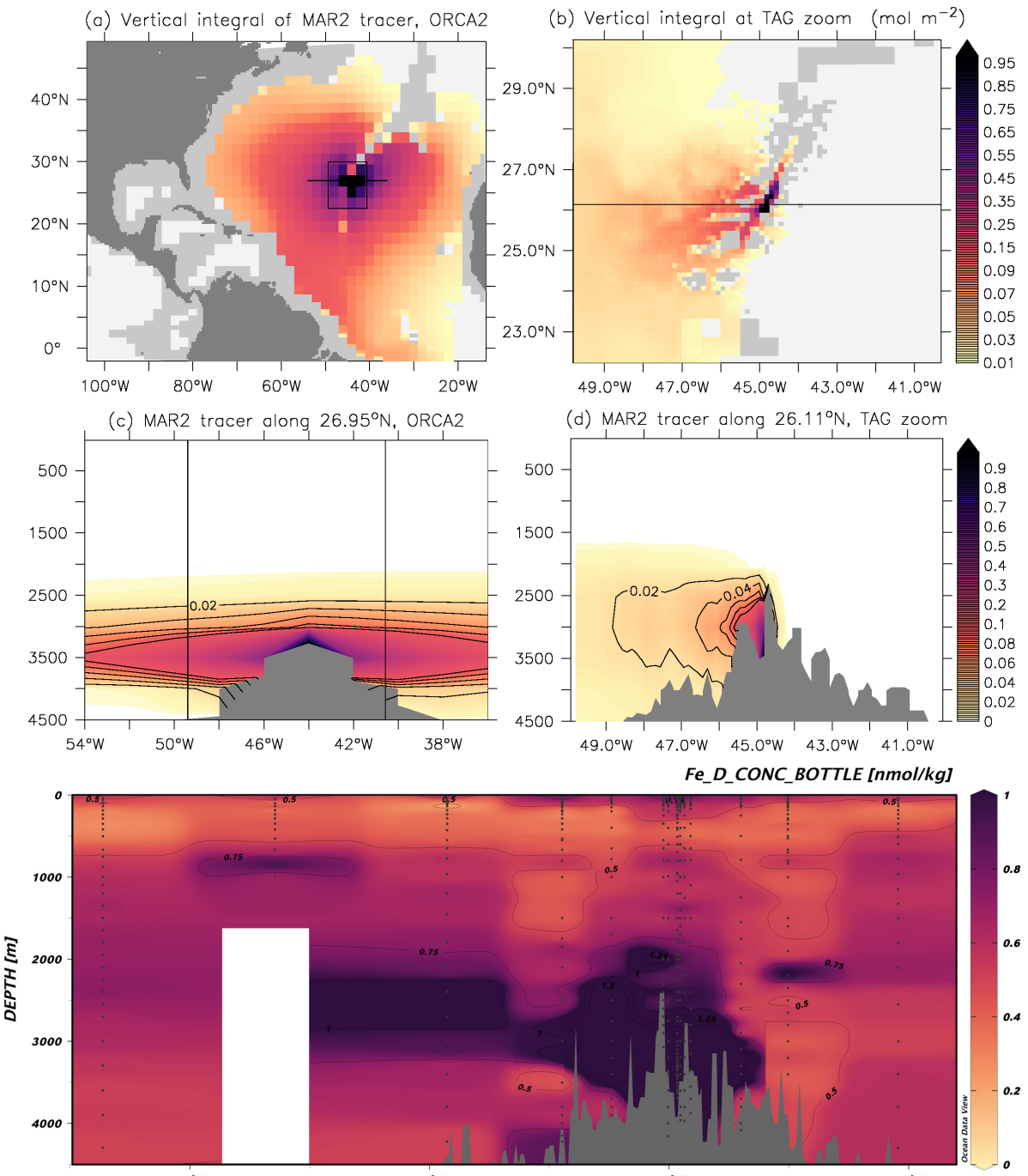


594

595   Figure 1. Vertical profiles of dissolved Fe (nM, black line, bottom x-axis), percentage  
596   of dFe present as soluble Fe (% red line, top x-axis) and the iron profile from a  
597   reference station (station 32, red dots, nM) for the range of stations within and outside  
598   the axial valley. The left-hand column shows stations within the valley, the central  
599   column shows stations from the west and the rightmost column shows stations to the  
600   east. Consult the map and supplementary figure 1 for more information on the  
601   stations and their spacing. Distances noted on each panel are the km from TAG.  
602  
603



604  
605  
606 Figure 2. Probability density function of particle presence after (a) 10, (b) 30, (c) 60,  
607 (d) 90, (e) 120 and (f) 180 days of dispersion from TAG (white circle). Individual  
608 positions are binned onto a 0.1-degree resolution grid. Green circles are the Fridge  
609 stations.  
610  
611



612

613

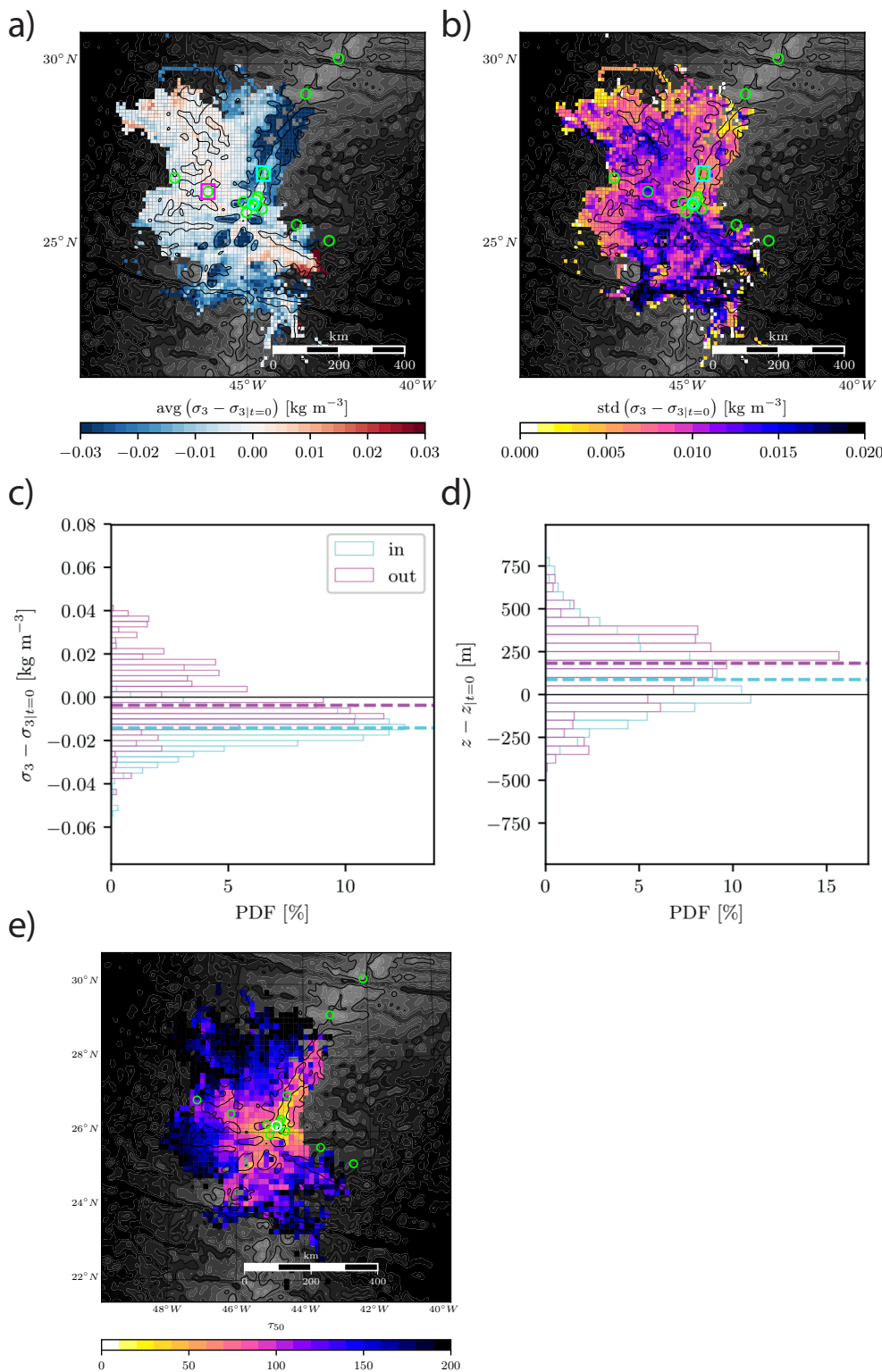
614 Figure 3. Vertically integrated tracer concentrations from an idealised tracer released  
 615 from TAG in two model configurations: (a) the coarse global ORCA2 configuration  
 616 and (b) a nested high-resolution AGRIF configuration. Panels (c) and (d) represent  
 617 the tracer concentrations along a zonal section for the ORCA and AGRIF  
 618 configurations, respectively. Panel (e) displays the merged GEOTRACES DFe  
 619 concentration data (nmol/kg) from the GA03 and GA13 voyages that crossed the  
 620 same region.

621

622

623

624



625

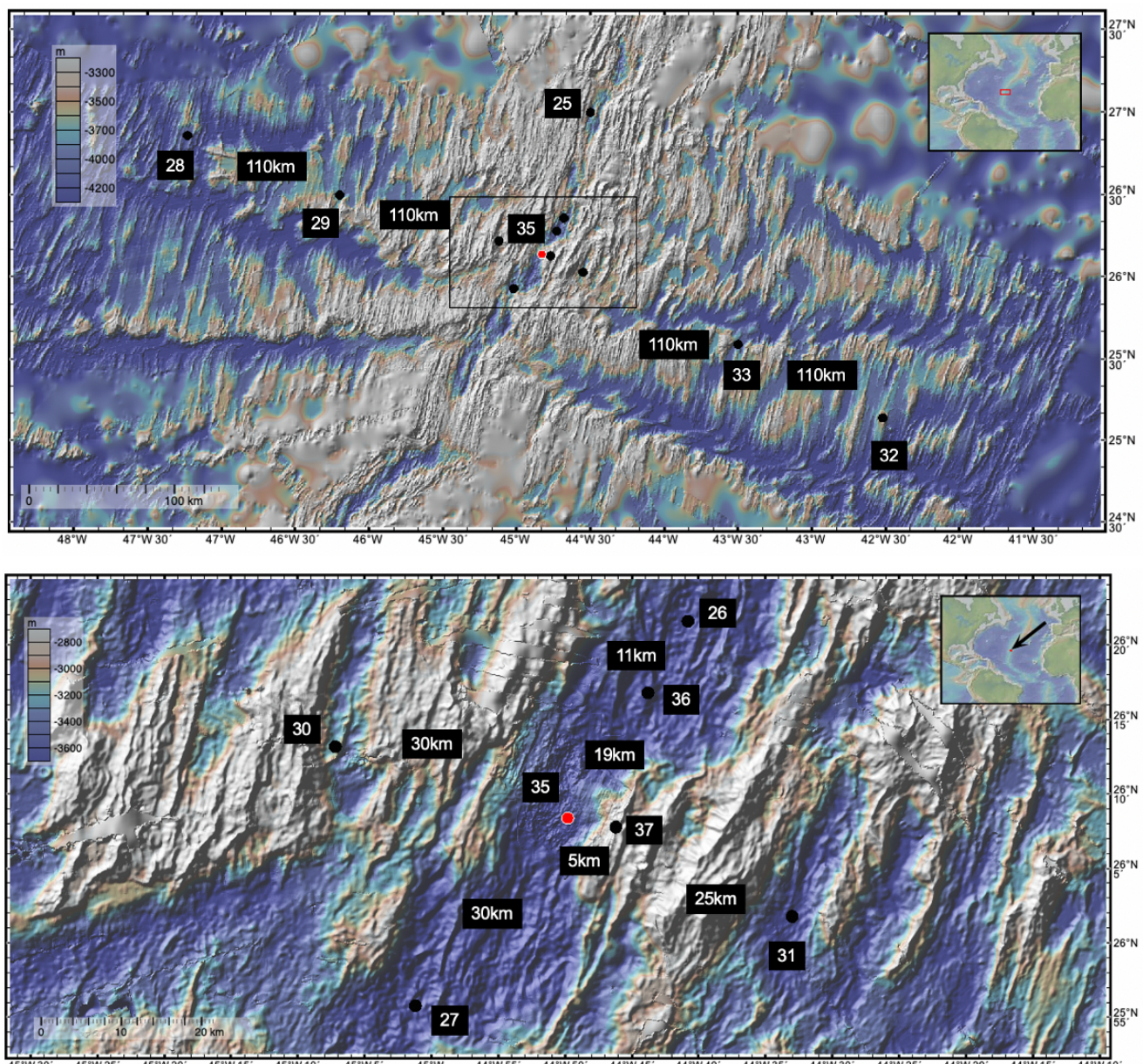
626 Figure 4. a) mean and b) standard deviation of the cumulative density change  
 627 relative to initial density. Panels c) and d) represent histograms of density and  
 628 absolute depth for particles inside and outside the valley (see squares on map on

629 panel a). e) Median ages (in days) of particles at the depth of maximum particle  
630 density after 6 months of model simulation  
631  
632

633    Supplementary Figures

634

635

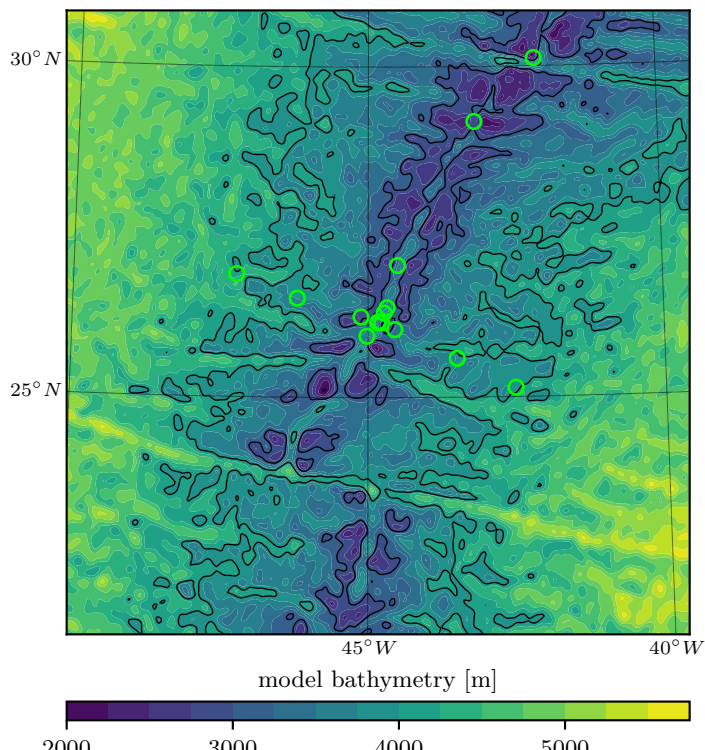


636

637

638 Supp Fig 1. JC156 Cruise stations. Red circle marks TAG at station 35 and labels  
 639 represent the spacing between stations. The closest station spacing is between 5-  
 640 30km close to TAG and extends to 110km further off axis. Upper panel shows the full  
 641 domain around the TAG site and the lower panel zooms in on stations immediately  
 642 adjacent to TAG enclosed by the black square.  
 643

644

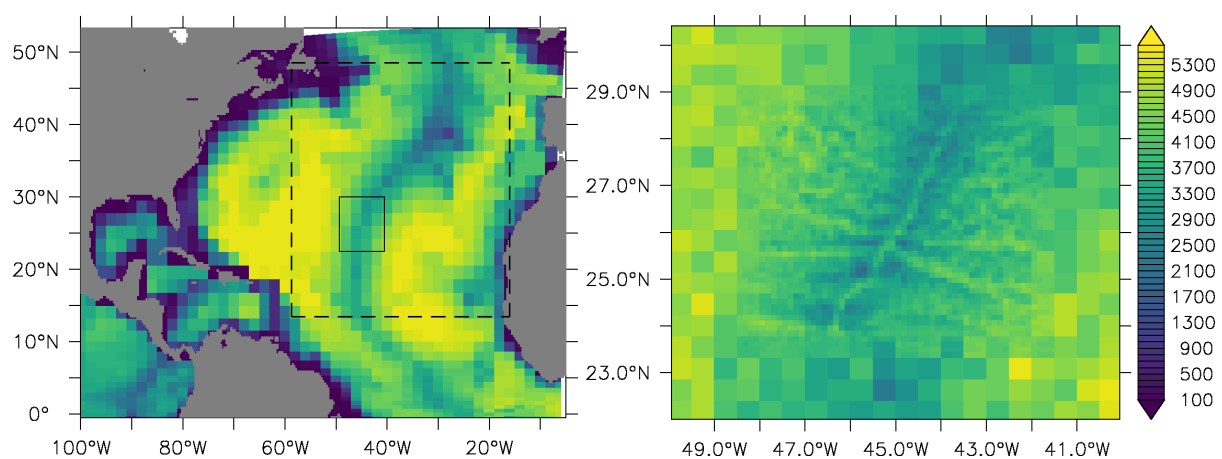


645

646 Supp Fig 2. Bathymetry in the GIGATL3 model with the GA13 sampling locations as  
647 green circles.

648

649



650

651

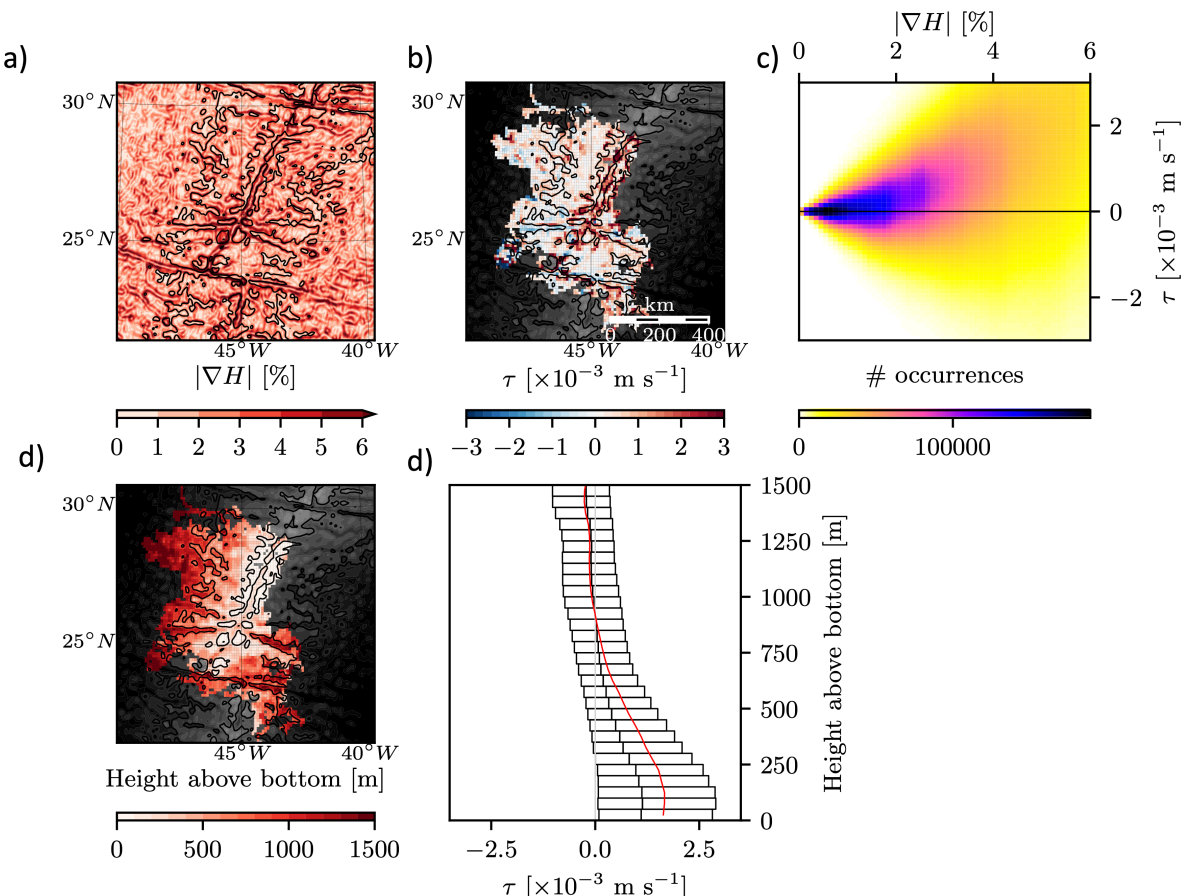
652

653 Supp Fig 3. Bathymetry in the ORCA2 and the AGRIF nested model configuration.

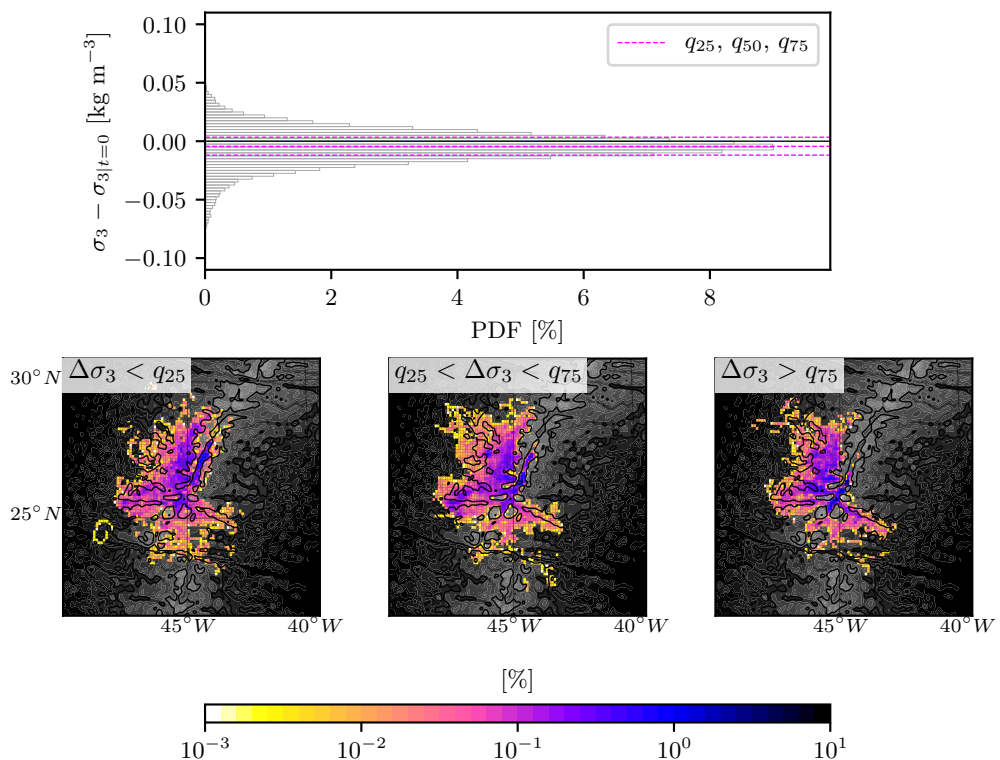
654 The AGRIF nesting is at 0.5x0.5 degrees (dashed box) and at 1/8 x1/8 degrees

655 (black box)

656



657  
 658  
 659 Supp Fig 4. Diagnostics related to topostrophy. (a) slope of bathymetry (grad(H)) (b)  
 660 topostrophy ( $\tau$ ) computed along particle trajectories and bin-averaged (c) Histogram  
 661 of  $\tau$  vs grad(H) (d) Bin-averaged height above bottom of particles and (e) quartiles  
 662 and mean of in height-above-bottom coordinates.  
 663  
 664



665  
 666  
 667 Supp Fig 5. (Top) histogram of density change and (bottom) histogram of position  
 668 discriminated on density change for all particles. Lower panels show maps of the  
 669 different distributions according to the density change quartile: (Left, lower quartile)  
 670 the 25% of particles that have lightened the most, (middle, middle quartile) 50% of  
 671 the particles that have shown the least change in density (i.e. in the middle of the  
 672 histogram) and (right, upper quartile) the 25% of the particles that have become  
 673 most dense.

674  
675  
676